



Geophysical Research Letters

RESEARCH LETTER

10.1029/2018GL077486

Kev Points:

- High-resolution images of Vs and Vp/Vs along a profile in NE Tibet were obtained from a joint inversion with Vp constraints
- The geological blocks are characterized by distinct seismic features with correlated crustal and mantle lithosphere structure
- Deformation is both continuous and localized and occurs at lithospheric scale

Supporting Information:

Supporting Information S1

Correspondence to:

Y. Deng, J. Li, and X. Song, yangfandeng345@gmail.com; jli109@illinois.edu; xiao.d.song@gmail.com

Citation:

Deng, Y., Li, J., Song, X., & Zhu, L. (2018). Joint inversion for lithospheric structures: Implications for the growth and deformation in northeastern Tibetan Plateau. *Geophysical Research Letters*, 45. https://doi.org/10.1029/2018GL077486

Received 7 FEB 2018 Accepted 16 APR 2018 Accepted article online 27 APR 2018

Joint Inversion for Lithospheric Structures: Implications for the Growth and Deformation in Northeastern Tibetan Plateau

Yangfan Deng^{1,2} D, Jiangtao Li² D, Xiaodong Song^{2,3} D, and Lupei Zhu⁴ D

¹State Key Laboratory of Isotope Geochemistry, Guangzhou Institute of Geochemistry, Chinese Academy of Sciences, Guangzhou, China, ²Department of Geology, University of Illinois at Urbana-Champaign, Champaign, IL, USA, ³School of Geodesy and Geomatics, Wuhan University, Wuhan, China, ⁴Department of Earth and Atmospheric Sciences, Saint Louis University, St. Louis, MO, USA

Abstract Several geodynamic models have been proposed for the deformation mechanism of Tibetan Plateau (TP), but it remains controversial. Here we applied a method of joint inversion of receiver functions and surface wave dispersions with *P* wave velocity constraint to a dense linear array in the NE Tibet. The results show that the geological blocks, separated by major faults at the surface, are characterized by distinct features in the crust, the Moho, and the uppermost mantle. The main features include crustal low-velocity zones (LVZs) with variable strengths, anomalous Vp/Vs ratios that are correlated with LVZs, a large Moho jump, and other abrupt changes near major faults, strong mantle lithosphere anomalies, and correlation of crustal and mantle velocities. The results suggest a lithospheric-scale deformation of continuous shortening as well as localized faulting, which is affected by the strength of the lithosphere blocks. The thickened mantle lithosphere can be removed, which facilitates the formation of middle-lower crustal LVZ and flow. However, such flow is likely a consequence of the deformation rather than a driving force for the outward growth of the TP. The proposed model of TP deformation and growth can reconcile the continuous deformation within the blocks and major faults at the surface.

Plain Language Summary How did the Tibetan Plateau grow to its present height and size? Models have been controversial for decades, including end-members of continuous deformation, rigid block extrusion, and channel flow in middle-lower crust. Here we used a recently developed joint inversion scheme to resolve several key seismic parameters simultaneously in a self-consistent manner for a linear array in the northeast margin of the plateau, which is ideal for testing models for the plateau growth. Our joint inversion results show distinct block-like features, which suggest a lithospheric-scale deformation of continuous shortening as well as localized faulting at the lithospheric scale. The proposed model of Tibetan Plateau deformation and growth can reconcile the continuous deformation within the blocks and major faults at the surface.

1. Introduction

As a margin of the vast Tibetan Plateau (TP) far away from the Indian-Asian collision front with devastating earthquakes, the northeast (NE) Tibet (Figure 1) has drawn close attention on the mechanism of the plateau uplift and growth after the collision started at about 55 Ma (Molnar & Tapponnier, 1975). Bounded by relatively stable North China Craton (NCC) to the north, NE TP is characterized by blocks of mountain ranges along the NW-SE strike, including Songpan-Ganzi Terrain (SGT), Kunlun-Qaidam Terrain (KQT), Central Qilian (CQL), and North Qilian (NQL), which are deforming continuously at the surface (Zhang et al., 2004) but are also separated by several major active thrust and sinistral strike-slip faults, including Kunlun fault (KF), South Qilian suture (SQS), Haiyuan fault (HF), and Gulang fault (GF; Figure 1).

Like elsewhere in TP, various models have been proposed for the deformation and growth mechanism in NE TP, including the continuous shortening (England & Houseman, 1986; Zhang et al., 2004), rigid block extrusion (Tapponnier et al., 2001), crustal channel flow (Clark & Royden, 2000), and integrated block and channel flow (Liu et al., 2014), but it remains controversial. Widespread midcrustal low-velocity zones (LVZs; Bao et al., 2013; Li et al., 2014) and low resistance zones (Le Pape et al., 2012) are observed in SGT that penetrate KF, consistent with the channel flow model. However, isolated LVZs are observed under Qilian (Bao et al., 2013; Li et al., 2014), which favors continuous shortening as a deformation

©2018. American Geophysical Union. All Rights Reserved.

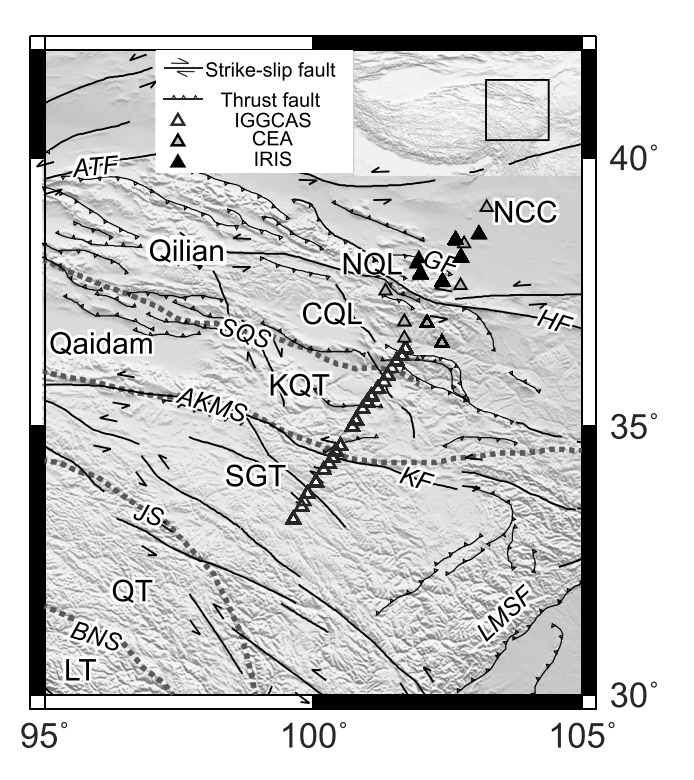


Figure 1. Seismic stations (triangles) used in this study with surface topography and geological elements. The stations were from IGGCAS (Institute of Geology and geophysics, Chinese Academy of Sciences), CEA (China Earthquake Administration), and IRIS (Incorporated Research Institutions for Seismology). The faults and sutures are as follows: ATF, Altyn Tagh fault; BNS, Bangong-Nujiang suture; JS, Jinsha suture; AKMS, Animaqing-Kunlun-Muztagh suture; SQS, South Qilian suture; KF, Kunlun fault; GF, Gulang fault; HF, Haiyuan fault; LMSF, Longmenshan fault. The geological blocks are as follows: LT, Lhasa terrane; QT, Qiangtang terrane; SGT, Songpan-Ganzi terrane; KQT, Kunlun-Qaidam terrane; CQL, Central Qilian; NQL, North Qilian; NCC, North China Craton.

mechanism (Gao et al., 2013). Furthermore, observed Moho offsets (Liu et al., 2017; Vergne et al., 2002; Ye et al., 2015; Zhu & Helmberger, 1998) and the correlation between Global Positioning System and SKS splitting (Chang et al., 2017; Soto et al., 2012; Wang, Zhao, et al., 2008) favor a coupled lithosphere-scale deformation (Tapponnier et al., 2001; Ye et al., 2015; Yin et al., 2008).

To shed light on the deformation and growth mechanism, here we applied a joint inversion scheme we recently developed (Li et al., 2017) to a dense seismic array in NE Tibet. We added *P* wave velocity constraint to the traditional joint inversion of surface wave dispersion and receiver function (RF; Julia et al., 2000) and adopted a flexible parameterization of a sedimentary layer and spline-based parameterization that can represent sharp discontinuities. The new joint inversion scheme reduced model ambiguity and allowed us to resolve crustal *S* velocity, thickness, and Vp/Vs velocity ratio simultaneously. The high-resolution images suggest the lithospheric-scale deformation and growth in NE Tibet involving both continuous shortening and localized faulting.

2. Data and Methods

2.1. Data

The data used in this study include three types, RFs, *P* wave velocity (Vp) model of the crust, and dispersion curves of surface wave group and phase velocities. These data were assembled roughly along a linear array spanning the interior of the TP and the stable NCC (Figures 1 and S1a in the supporting information).

The RF data came from 37 broadband stations. In the southern part of the array (south of Xining), 22 stations were deployed along a line with the interval of 10–15 km by the Institute of Geology and Geophysics, Chinese Academy of Sciences (IGGCAS) between November 2010 and June 2011 (Xu et al., 2014). To extend the array to the north, we obtained data (08/2007–10/2009) from eight permanent stations operated by the Chinese Earthquake Administration (CEA; Tian et al., 2014; Zheng et al.,

2010) and data (03/2009–07/2010) from seven Incorporated Research Institutions for Seismology (IRIS) stations from a temporary deployment NETS (Shen et al., 2008). To calculate the RFs, we selected teleseismic P waveforms from earthquakes with magnitudes $M_w \geq 5.5$ and in the epicentral distance range from 30° to 90°. We used a time domain iterative deconvolution method (Ligorría & Ammon, 1999) to obtain the RFs. Specifically, we performed a quality control process (Deng et al., 2015; Shen et al., 2013) on the raw RFs of all the 37 stations. Finally, we used the RFs at their Moho piercing points and stacked them at stacking points of an even interval of 20 km (Figure S1a) to enhance further the signals and to average out the influences from the uneven distributions of data azimuths and stations (Deng et al., 2015). The RFs after the quality control (examples in Figure S2) show significant improvement on the consistency of the signals over the raw RFs; see examples in Xu et al. (2014). The main features in the stacked RF can be tracked in the selected raw RFs. We used the standard deviations of the selected raw RFs as the error bound (uncertainty) of the stacked RF.

Our Vp model for the southern part of the array (Figure S1c) came from a 380-km-long deep seismic sounding profile (deep seismic sounding or wide-angle reflection-refraction survey with active sources), which was carried out by the IGGCAS over a 4-month period in 2003 (Zhang et al., 2011). A total of 100 portable three component digital seismographs were installed at the average spacing of 3 to 4 km and the offset of 3 to 390 km. Five explosive charges of 3,000–3,500 kg were fired at the spacing of about 80 km. The data were initially recorded at 200-Hz sampling rate and then filtered at 1–10 Hz band for the *P* waves. See Zhang et al. (2011) for details on the data processing and model construction.



The dispersion data came from our recent surface wave tomography of China (Bao et al., 2015) using both ambient noise and earthquake data. The stations included 864 CEA permanent stations from 2008 to 2011, 401 temporary PASCCAL stations, and 51 permanent stations from the IRIS Data Management Center. More than 700,000 dispersion curves were measured to generate group and phase velocity maps at periods of 10–70 s (as well as group velocity maps extending to 140 s). In this study, we extracted group and phase velocity dispersion curves at each of our stacking points from the dispersion maps of 10–70 s, which were better constrained with both the ambient noise and earthquake data.

2.2. Method

Details of the new joint inversion scheme with P velocity constraints were described in Li et al. (2017). Here we briefly summarize the method. The teleseismic P wave RF is sensitive to shear velocity contrast and depth-velocity product, instead of velocity alone, while the surface wave dispersion is sensitive to vertical shear-velocity averages but insensitive to velocity discontinuities. Thus, joint inversion of RF and surface wave dispersion has been widely used to reduce parameter ambiguity in the inversion (Julia et al., 2000). However, the joint inversion is greatly influenced by the Vp/Vs ratio in the crust, which is often unconstrained and normally set to the global average (1.75). Multiple converted phases (the well known H-k method) can help resolving the ambiguity (Zhu & Kanamori, 2000), but with its limitations (Li et al., 2017). Thus, Li et al. (2017) introduced a P velocity model into the traditional joint inversion of P wave RF and surface wave dispersion to reduce model ambiguity and to obtain of Vs structure, Moho and intracrustal discontinuities, and crustal Vp/Vs profile simultaneously. The method was implemented using a global search-based algorithm and a flexible parameterization of a sedimentary layer and spline-based parameterization that can represent sharp discontinuities. The inclusion of a sedimentary layer is important to fit the beginning part of RFs; an inversion without it may result in artifacts in both shallow and deep crust. The method works for a variety of crustal models, including thin/thick sedimentary layer, LVZ/high-velocity zone (HVZ), sharp/gradual Moho, or fast/slow mantle.

Li et al. (2017) applied the method to a profile in SE TP, where the Vp model was extracted from a 3-D regional tomographic model. Ye et al. (2017) applied it to a dense profile across the eastern margin of the TP, where the Vp model was independently derived from an active refraction survey along the same profile.

In this study, we applied the joint inversion with Vp constraints to the profile in NE TP. In the southern part of the profile, where the active source refraction survey was conducted, we used the independently derived *P* wave velocity model, just like in Ye et al. (2017). Two examples of the joint inversion with using real data are shown in Figure S3 under SGT and CQL, respectively.

In the northern part of the array, no *P* velocity profile is available. We fixed the averaged Vp/Vs ratios according to the averaged values for the different blocks (1.72 to 1.79) of the southern part. Two examples are shown in Figure S4 under NQL and NCC, respectively. The results with different Vp/Vs ratios vary in minor details but show general consistent features. We chose the final Vp/Vs values for different blocks of the northern part according to the general Vs characteristics between the northern and the southern blocks, that is, keeping it the same in CQL (1.72, from the southern part of CQL), using the value of KQT (1.75) for NQL, and using the value of CQL (1.72) for NCC (Figure S4).

3. Results

The joint inversion results show not only variable crustal properties among the geological blocks but also considerable consistency within each block (Figure 2). The Moho depth generally decreases from around 60 km in SGT to 50 km in NCC (Figure 2c). A sharp jump of Moho is observed from CQL to NQL (beneath HF) by as much as 15 km. Crustal LVZs exist in all blocks with decreasing strength from south to north in general. The LVZs appear as narrow patches of varying strengths at different depths. LVZs are strongest and broadest in SGT but much weaker in CQL and NCC. Anomalously high Vp/Vs ratios are observed in the middle-lower crust in SGT and KQT (Figure 2d), corresponding to LVZs at the same locations (Figure 2c). Abrupt changes are observed near the major faults, including SQS (middle-lower crust LVZs and mantle velocity, Moho), HF (the Moho, mantle velocity), and GF (middle-lower crust LVZ and HVZ, mantle velocity, Moho). However, some features are continuous across the faults, in particular, the midcrust LVZ across KF and HF and the lower crust HVZ in KQT-CQL.

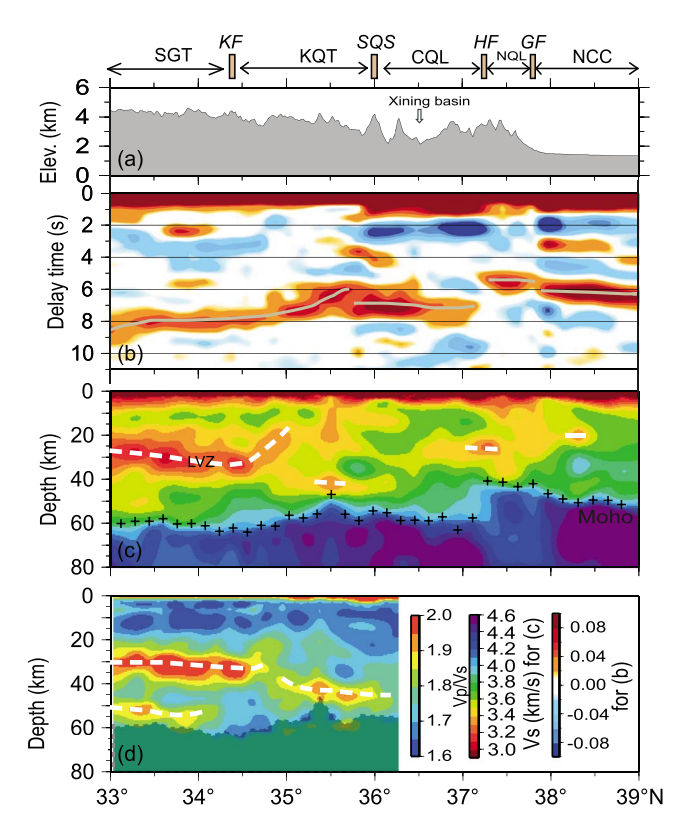


Figure 2. Results of our joint inversion. (a) Topography and geological elements along the profile. (b) Receiver function (RF) image along the profile. P-to-S converted phases are marked by gray solid lines. (c) Vs profile from joint inversions. The southern part is from the joint inversion of RF, dispersion, and Vp. The northern part is from the joint inversion of RF, dispersion, and fixed Vp/Vs ratios (see section 2.2). Prominent low-velocity zones and the Moho are marked with white dashed lines and crosses, respectively. (d) Vp/Vs profile from the joint inversion of RF, dispersion, and Vp. The white dashed lines mark the high Vp/Vs zone. The shading region indicates that the Vp/Vs is not from the inversion. The uncertainties of (c) and (d) are shown in Figure S6.

In general, a rapid velocity decrease/increase with depth (LVZ/HVZ) appears as negative/positive amplitude in the RF. We see clear patches of negative or positive amplitude in the RF image (Figure 2b) between 2 s and the Moho, corresponding to the LVZs or HVZs in the crust (Figures 2b and 2c). The Moho discontinuity across HF is also striking in the RFs with a jump of nearly 2 s. A smaller but clear difference (time shift of about 0.5 s) is observed at the Moho across GF.

The Vs in the uppermost mantle shows strong variation as well. It is slow under SGT, NQL, and southern KQT, while fast under NCC, CQL, and northern KQT. The changes across GF and HF are rather abrupt (see also discussion below), while the changes across KF and SQS are more gradual.

4. Discussion

4.1. Robustness of Joint Inversion Results

Extensive tests from Li et al. (2017) using synthetic and real data demonstrate that the method is robust for a variety of crustal and mantle velocity structures and intracrustal and Moho discontinuities, including the recovery of sedimentary layer, Moho depth, crustal LVZ or HVZ, Vp/Vs variation with depth, and fast or slow mantle structure. The joint inversion method uses only the crustal part of P velocity model beneath the station, which is fixed as an input constraint. Ye et al. (2017) tested the influence of the uncertainty of the input Vp model (within 0.1 km/s) on the resulting models of the joint inversion and demonstrated that the main pattern of the final Vs and Vp/Vs models of the joint inversion is not affected. This is also clear when we tested joint inversions with different average Vp/Vs values assumed for the crust (Figure S5). Within a reasonable range of Vp/Vs ratios (1.72 to 1.79), the resulting Vs profiles show general consistent features with minor difference in details. We have also estimated uncertainties of the joint inversion (Figure S6) based on our model search results. The errors in S velocity and Vp/Vs ratio are within 0.1 and 0.03 km/s, respectively.

As Vp in the crust is fixed in the joint inversion, any errors in the Vp model would also be mapped directly to errors in the Vp/Vs ratio, not just affecting its patterns. In *P* wave refraction profiles, crustal layering of 0.1 km/s

increment can typically be resolved (e.g., Jia et al., 2010; Liu et al., 2006; Zhang et al., 2011, 2013); thus, we may regard 0.1 km/s as vertical resolvability in such a survey. Anomalously high Vp/Vs ratios are observed in the middle-lower crust in SGT and KQT, which are correlated with Vs LVZs at the same locations (Figure 2). However, in the Vp profile, there are no strong LVZs in the middle-lower crust. For example, at the location of stacking point 3 in SGT (Figure S1), where Vs decreases from 3.57 to 3.20 km/s (10.4%) in midcrust, Vp decreases only slightly from 6.01 to 5.92 km/s (1.5%). In other refraction profiles in NE TP, pockets of LVZs in Vp can be clearly observed in middle-lower crust with Vp decreasing by 0.1 to 0.2 km/s (over the Vp of about 6.0 km/s, or less than 4% decrease; Jia et al., 2010; Liu et al., 2006; Zhang et al., 2013). Thus, we believe that the anomalous Vp/Vs ratios come mainly from Vs anomalies.

4.2. Correlation Between Crust and Mantle in Velocity Structure

Figure 2 shows that low/high velocity in the crust generally corresponds to low/high velocity in the mantle. To quantify the correlation, we calculate the average velocity in the crust (from 4 km below the sedimentary layer to Moho) and uppermost mantle (top 20 km). The positive correlation between the crustal velocity variation and that of the uppermost mantle is a common feature in all the blocks of the NE TP (Figure 3). The average velocities of both the crust and uppermost mantle increase from SGT (lowest) to CQL, decrease in NQL, and increase again in NCC (highest). The surface topography of CQL is more rugged than that of SGT and KQT (Figure 2a). The Xining basin in CQL is underlain by basement and mantle lithosphere of fast velocities. Based on these features, we characterize the lithosphere strength of the blocks SGT to NCC from south

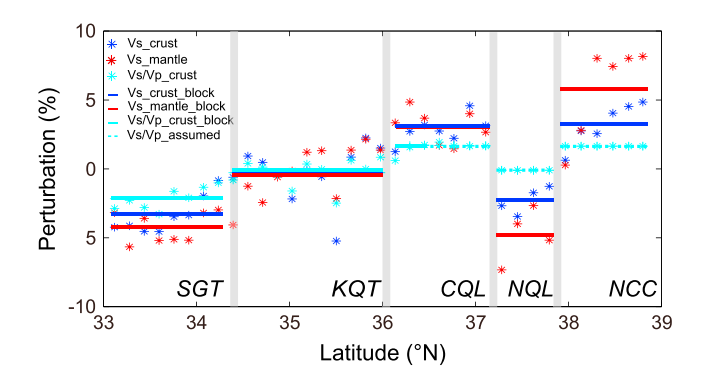


Figure 3. Perturbations of Vs and Vs/Vp. The ratio Vs/Vp is used, instead of the conventional Vp/Vs, to show better correlation with versus the perturbations (relative to the mean of all data points) of Vs in the crust (blue), Vs in the uppermost mantle (top 20 km; red), and Vs/Vp in the crust (cyan) for each stacking point (star; Figure 2b), and their averages for each block (line) are plotted. The crustal values exclude the sedimentary layer. The Vs/Vp values (dashed lines) for North China Craton, North Qilian, and northern part of Central Qilian were assumed as section 2.2 described.

to north as weakest (SGT), weak (KQT), strong (CQL), weak (NQL), and strongest (NCC). Note we have previously examined extensively possible trade-offs between crust and mantle structures (Li et al., 2017) for a variety of models. The crustal and mantle structure can be resolved simultaneously in the joint inversion.

4.3. Mechanism for Plateau Growth and Deformation

The crustal LVZs (Figure 2c), which show high Vp/Vs ratios where available (Figure 2d), are consistent with partial melting (Hacker et al., 2014). However, the LVZs vary in strength in different blocks. The LVZ distribution does not correlate with the crustal thickness. The thickness is similar in SGT and CQL, and a midcrust LVZ cuts across the HF where the Moho has a jump. The correlation of crustal and uppermost mantle velocities also suggests that the crust and mantle are coupled as a lithosphere block. Consistent with geodynamic modeling, the continuous collision and lithospheric-scale variations play an important role in the formation of LVZs (Chen & Gerya, 2016). In conclusion, our observations suggest that the middle-lower crustal channel flow model is unlikely the main mechanism for crustal thickening and plateau growth (Clark & Royden, 2000).

The observations are best explained by a lithospheric-scale deformation mechanism involving both continuous shortening and localized faulting (Figure 4). We propose that the northeastern expansion of the TP in Neogene (Wang, Flesch, et al., 2008; Yin et al., 2008) is primarily through continuous lithosphere-scale shortening (Zhang et al., 2004, 2014), in which the strength of the lithosphere plays a key role in the shortening process with weaker blocks deforming more easily. However, localized deformations along major faults (Tapponnier et al., 2001) accommodate part of the India-Eurasian shortening as well as lateral material extrusion, which is also likely lithosphere scale as evidenced previously (Chang et al., 2017; Holt, 2000; Ye et al., 2015; Zhu & Helmberger, 1998) and here by the Moho or near Moho changes across SQS, HF, and GF. The thickened mantle lithosphere can be delaminated (Bird, 1979) or convectively removed (Molnar et al., 1993). Our results show patches of fast and slow anomalies in the mantle (Figure 4). The mantle lithosphere in SGT and southern KQT has probably been removed with traces of delaminated pieces. The mantle lithosphere in CQL and northern KQT is currently undergoing delamination with some residual mantle lithosphere remaining. Much of the mantle lithosphere in NQL has also been removed perhaps together with the base of the crust, giving rise to the sudden decrease of the Moho depth. The interpretation is consistent with the rapid uplift of the Qilian block at Miocene-Quaternary from recent high-resolution magnetostratigraphy and tectonosedimentology (Fang et al., 2013). The mantle lithosphere at the southern edge of NCC has also started to be eroded. Volcanism in NE TP is not common, but there is exposure of young volcanic rocks (<6 Ma) in the west part of North Qilian Mountains (Xia et al., 2011).

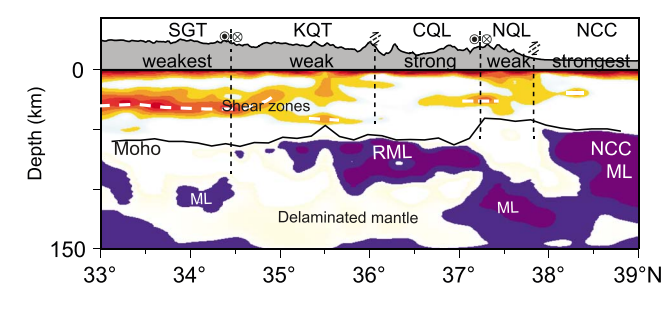


Figure 4. Interpretative illustration for the proposed deformation mechanism in NE Tibet. The color patches outline the lowest velocities in the crust and highest velocities in the mantle from our joint inversion results. The fault mechanisms are referred to Taylor and Yin (2009). The main features include lithosphere blocks (vertical dashed lines with the main fault motions), prominent crustal shear zones (low-velocity zones), mantle lithosphere (ML) with traces of residual mantle lithosphere (RML), and delaminated mantle lithosphere.

The middle-lower crust is highly deformed in SGT-KQT, and the process has started at the edge of QL and NCC (Figure 4). The middle-lower crust LVZs may form as horizontal shear zones from the crust thickening and intense deformation (Nabelek et al., 2010). However, the excellent correlation between the middle-lower crustal LVZs and the scale of delamination in the mantle suggest that the elevated temperature and mantle upwelling after the delamination may have played a great or controlling role in the formation and size of the LVZs (Bird, 1979; Molnar et al., 1993). The amplitude and scale of the shear zone may indicate the stage of the lithosphere deformation and delamination as well as its strength. The large midcrust LVZ in SGT and KQT reflects its longer history of deformation, which may have become ductile enough to flow, resulting in the flatter surface and Moho topography (Bird, 1991) in SGT. Such flow, however, is not the driving mechanism of the outward growth of the TP; rather, it is a consequence of the continuous deformation, and it is localized to the affected areas. The gradual northward LVZs in QL and NCC and other



smaller and isolated pockets of LVZs may indicate the initial stage of their formations (Bao et al., 2013).

The model may be broadly applicable to other parts of the plateau as a possible common mechanism for intracontinental deformation. For example, in a recent joint inversion of Rayleigh dispersions and RFs in NE TP, Zheng et al. (2016) show similar trends near our profile: thinner crust beneath NQL, generally decreasing Vp/Vs (or increasing Vs/Vp) from SGT northwards to NCC, and low velocity in SGT, KQT, and NQL and high velocity in CQL in the uppermost mantle. Shi et al. (2017) reported crustal block-like features in NE margin of TP from RFs of two dense seismic profiles across the Qilian Mountains. They proposed that the weaker Qilian orogen is squeezed up by more rigid blocks in the north (NCC block) and the south (Qaidam block) to cause elevated arch-like Moho. However, consistent with our model, we provide an alternative interpretation that the shallower Moho is caused by buoyancy from mantle lithosphere delamination. Along Shi et al.'s West Line, the uppermost mantle is rather slow (see Figure 4c of Bao et al., 2013). Shi et al.'s East Line is very close to our profile. The Moho is only elevated in NQL (north of HF), which is consistent with our imaging result (Figure 2c) and is caused by mantle delamination under NQL according to our interpretation. However, as Shi et al. has dense station distribution, the Moho change across HF appears continuous; that is, the offset may not be sharp right at HF as it appears in our study (Figure 2c), but over a short distance. Nevertheless, the large depth offset between the two blocks across HF is clear in both studies. Elsewhere, Ye et al. (2017) found a correlation between crust and uppermost mantle velocities along a dense profile in E. Tibet. Similarly, in SE Tibet, Liu et al. (2014) found correspondence between prominent low-velocity region in the crust and low-velocity uppermost mantle (interpreted as the transitional crust-mantle). In western Tibet, Zhang et al. (2014) found that the major tectonic blocks are bounded by faults or shear zones that cut through the crust to the Moho and that the segmentation of the Tibetan crust is compatible with a shortening deformation.

5. Conclusions

We applied the joint inversion scheme of RFs and dispersions with *P* velocity constraints to a dense profile in NE TP with both active and passive experiments. We obtained high-resolution images of Vs, Vp/Vs, and discontinuities simultaneously as well as the improved mantle Vs structure. The main features include the following: crustal LVZs with variable strengths, anomalous Vp/Vs ratios that are correlated with LVZs, large Moho jump across HF and other abrupt changes near major faults, correlation of crustal and mantle velocities, and strong mantle lithosphere anomalies.

The distinct features seem to suggest a lithospheric-scale deformation of continuous shortening and localized faulting, which is affected by the strength of the lithosphere blocks. Comparatively, SGT is weaker and has experienced stronger deformation, while CQL and NCC are stronger and are in the initial stage of significant deformation. The thickened mantle lithosphere from the lithospheric shortening can be delaminated or convectively removed, which appears most prominently under weaker blocks (SGT, KQT, and NQL). The middle-lower crust LVZs may form as the result of lithosphere delamination and intense deformation, which may be able to flow (Clark & Royden, 2000; Klemperer, 2006). However, such flow is not the driving mechanism of the outward growth of the TP; rather, it is a consequence of the continuous deformation. The proposed model of TP deformation and growth can reconcile the continuous deformation within the blocks observed by geodetic observations (Zhang et al., 2004) and localized deformation along major faults observed in major earthquakes and geological mapping (Tapponnier et al., 2001). The model may be applicable to other parts of the plateau as a possible common mechanism for intracontinental deformation.

The waveform data for the southern part were acquired by Xiaobo Tian, Tao Xu, Zhiming Bai, Changqing Sun, and Fei Li in the late Professor Zhongjie Zhang's group at Institute of Geology and Geophysics, Chinese Academy of Sciences (IGGCAS) and the waveform data for the northern part were obtained from China Earthquake Administration (CEA) and Incorporated Research Institutions for Seismology (IRIS). The receive function data are available upon request from the corresponding author. We appreciate the comments from two anonymous reviewers, which improved the manuscript. The authors benefited from discussions with An Yin and Greg Houseman. The data used (dispersion, RF, and Vp) and the models obtained (Vs, Vp/Vs, and Moho depth) in this study are available at https://www. researchgate.net/publication/ 324224188_The_data_for_GRL_paper. The research was supported by the Strategic Priority Research Program (B) of the Chinese Academy of Sciences (XDB18000000), the National Nature Science Foundation of China (41504069 and 41774056), the China National Special Fund for Earthquake Scientific Research in Public Interest (201508020). and the U.S. National Science Foundation (EAR 1620595).

Acknowledgments

References

Bao, X., Song, X., & Li, J. (2015). High-resolution lithospheric structure beneath Mainland China from ambient noise and earthquake surface-wave tomography. Earth and Planetary Science Letters, 417, 132–141. https://doi.org/10.1016/j.epsl.2015.02.024

Bao, X., Song, X., Xu, M., Wang, L., Sun, X., Mi, N., et al. (2013). Crust and upper mantle structure of the North China Craton and the NE Tibetan Plateau and its tectonic implications. *Earth and Planetary Science Letters, 369-370,* 129–137. https://doi.org/10.1016/j.epsl.2013.03.015 Bird, P. (1979). Continental delamination and the Colorado Plateau. *Journal of Geophysical Research, 84*(B13), 7561–7571. https://doi.org/10.1029/JB084iB13p07561

Bird, P. (1991). Lateral extrusion of lower crust from under high topography in the isostatic limit. *Journal of Geophysical Research*, *96*(B6), 10,275–10,286. https://doi.org/10.1029/91JB00370

Chang, L., Ding, Z., Wang, C., & Flesch, L. M. (2017). Vertical coherence of deformation in lithosphere in the NE margin of the Tibetan Plateau using GPS and shear-wave splitting data. *Tectonophysics*, 699, 93–101. https://doi.org/10.1016/j.tecto.2017.01.025



- Chen, L., & Gerya, T. V. (2016). The role of lateral lithospheric strength heterogeneities in orogenic plateau growth: Insights from 3-D thermomechanical modeling: 3-D modeling of orogenic plateau growth. *Journal of Geophysical Research: Solid Earth, 121*, 3118–3138. https://doi.org/10.1002/2016JB012872
- Clark, M. K., & Royden, L. H. (2000). Topographic ooze: Building the eastern margin of Tibet by lower crustal flow. *Geology*, 28(8), 703–706. https://doi.org/10.1130/0091-7613(2000)28%3C703:TOBTEM%3E2.0.CO;2
- Deng, Y., Shen, W., Xu, T., & Ritzwoller, M. H. (2015). Crustal layering in northeastern Tibet: A case study based on joint inversion of receiver functions and surface wave dispersion. *Geophysical Journal International*, 203(1), 692–706. https://doi.org/10.1093/qjj/ggv321
- England, P., & Houseman, G. (1986). Finite strain calculations of continental deformation: 2. Comparison with the India-Asia collision zone. *Journal of Geophysical Research*, 91(B3), 3664–3676. https://doi.org/10.1029/JB091iB03p03664
- Fang, X., Liu, D., Song, C., Dai, S., & Meng, Q. (2013). Oligocene slow and Miocene–quaternary rapid deformation and uplift of the Yumu Shan and north Qilian Shan: Evidence from high-resolution magnetostratigraphy and tectonosedimentology. *Geological Society, London, Special Publications*, 373(1), 149–171. https://doi.org/10.1144/SP373.5
- Gao, R., Wang, H., Yin, A., Dong, S., Kuang, Z., Zuza, A. V., et al. (2013). Tectonic development of the northeastern Tibetan Plateau as constrained by high-resolution deep seismic-reflection data. *Lithosphere*. 5(6), 555–574. https://doi.org/10.1130/L293.1
- Hacker, B. R., Ritzwoller, M. H., & Xie, J. (2014). Partially melted, mica-bearing crust in Central Tibet. *Tectonics*, 33(7), 1408–1424. https://doi.org/10.1002/2014TC003545
- Holt, W. E. (2000). Correlated crust and mantle strain fields in Tibet. *Geology*, 28(1), 67–70. https://doi.org/10.1130/0091-7613(2000)28%3C67: CCAMSF%3E2.0.CO;2
- Jia, S., Zhang, X., Zhao, J., Wang, F., Zhang, C., Xu, Z., et al. (2010). Deep seismic sounding data reveal the crustal structures beneath Zoigê basin and its surrounding folded orogenic belts. Science China Earth Sciences, 53(2), 203–212. https://doi.org/10.1007/s11430-009-0166-0
- Julia, J., Ammon, C., Herrmann, R., & Correig, A. M. (2000). Joint inversion of receiver function and surface wave dispersion observations. Geophysical Journal International, 143(1), 99–112. https://doi.org/10.1046/j.1365-246x.2000.00217.x
- Klemperer, S. L. (2006). Crustal flow in Tibet: Geophysical evidence for the physical state of Tibetan lithosphere, and inferred patterns of active flow. *Geological Society, London, Special Publications*, 268(1), 39–70. https://doi.org/10.1144/gsl.sp.2006.268.01.03
- Le Pape, F., Jones, A. G., Vozar, J., & Wenbo, W. (2012). Penetration of crustal melt beyond the Kunlun fault into northern Tibet. *Nature Geoscience*, 5(5), 330–335. https://doi.org/10.1038/ngeo1449
- Li, H., Shen, Y., Huang, Z., Li, X., Gong, M., Shi, D., et al. (2014). The distribution of the mid-to-lower crustal low-velocity zone beneath the northeastern Tibetan Plateau revealed from ambient noise tomography. *Journal of Geophysical Research: Solid Earth, 119*, 1954–1970. https://doi.org/10.1002/2013JB010374
- Li, J., Song, X., Zhu, L., & Deng, Y. (2017). Joint inversion of surface wave dispersions and receiver functions with P-velocity constraints: Application to southeastern Tibet. *Journal of Geophysical Research: Solid Earth, 122*, 7291–7310. https://doi.org/10.1002/2017JB014135
- Ligorría, J. P., & Ammon, C. J. (1999). Iterative deconvolution and receiver-function estimation. *Bulletin of the Seismological Society of America*, 89(5), 1395–1400.
- Liu, M., Mooney, W. D., Li, S., Okaya, N., & Detweiler, S. (2006). Crustal structure of the northeastern margin of the Tibetan Plateau from the Songpan-Ganzi terrane to the Ordos basin. *Tectonophysics*, 420(1–2), 253–266. https://doi.org/10.1016/j.tecto.2006.01.025
- Liu, Q. Y., van der Hilst, R. D., Li, Y., Yao, H. J., Chen, J. H., Guo, B., et al. (2014). Eastward expansion of the Tibetan Plateau by crustal flow and strain partitioning across faults. *Nature Geoscience*, 7(5), 361–365. https://doi.org/10.1038/ngeo2130
- Liu, Z., Tian, X., Gao, R., Wang, G., Wu, Z., Zhou, B., et al. (2017). New images of the crustal structure beneath eastern Tibet from a high-density seismic array. Earth and Planetary Science Letters, 480, 33–41. https://doi.org/10.1016/j.epsl.2017.09.048
- Molnar, P., England, P., & Martinod, J. (1993). Mantle dynamics, uplift of the Tibetan Plateau, and the Indian monsoon. *Reviews of Geophysics*, 31(4), 357–396. https://doi.org/10.1029/93RG02030
- Molnar, P., & Tapponnier, P. (1975). Cenozoic tectonics of Asia: Effects of a continental collision. Science, 189(4201), 419–426. https://doi.org/10.1126/science.189.4201.419
- Nabelek, P. I., Whittington, A. G., & Hofmeister, A. M. (2010). Strain heating as a mechanism for partial melting and ultrahigh temperature metamorphism in convergent orogens: Implications of temperature-dependent thermal diffusivity and rheology. *Journal of Geophysical Research*, 115, B12417. https://doi.org/10.1029/2010JB007727
- Shen, W., Ritzwoller, M. H., Schulte-Pelkum, V., & Lin, F.-C. (2013). Joint inversion of surface wave dispersion and receiver functions: A Bayesian Monte-Carlo approach. *Geophysical Journal International*, 192(2), 807–836. https://doi.org/10.1093/gji/ggs050
- Shen, Y., Shi, D. N., Li, X. F., Sandvol, E., Li, A. B., & Li, H. Y. (2008). Northeast Tibet plateau seismic experiment. International Federation of Digital Seismograph Networks. Other/Seismic Network. https://doi.org/10.7914/SN/ZV 2008
- Shi, J., Shi, D., Shen, Y., Zhao, W., Xue, G., Su, H., & Song, Y. (2017). Growth of the northeastern margin of the Tibetan Plateau by squeezing up of the crust at the boundaries. *Scientific Reports*, 7(1), 10591. https://doi.org/10.1038/s41598-017-09640-0
- Soto, G. L., Sandvol, E., Ni, J., Flesch, L. M., Hearn, T. M., Tilmann, F., et al. (2012). Significant and vertically coherent seismic anisotropy beneath eastern Tibet. *Journal of Geophysical Research*, 117, B05308. https://doi.org/10.1029/2011JB008919
- Tapponnier, P., Zhiqin, X., Roger, F., Meyer, B., Arnaud, N., Wittlinger, G., & Jingsui, Y. (2001). Oblique stepwise rise and growth of the Tibet Plateau. Science, 294(5547), 1671–1677. https://doi.org/10.1126/science.105978
- Taylor, M., & Yin, A. (2009). Active structures of the Himalayan-Tibetan orogen and their relationships to earthquake distribution, contemporary strain field, and Cenozoic volcanism. *Geosphere*, *5*(3), 199–214. https://doi.org/10.1130/GES00217.1
- Tian, X., Liu, Z., Si, S., & Zhang, Z. (2014). The crustal thickness of NE Tibet and its implication for crustal shortening. *Tectonophysics*, 634, 198–207. https://doi.org/10.1016/j.tecto.2014.07.001
- Vergne, J., Wittlinger, G., Hui, Q., Tapponnier, P., Poupinet, G., Mei, J., et al. (2002). Seismic evidence for stepwise thickening of the crust across the NE Tibetan Plateau. Earth and Planetary Science Letters, 203(1), 25–33. https://doi.org/10.1016/S0012-821X(02)00853-1
- Wang, C., Zhao, X., Liu, Z., Lippert, P. C., Graham, S. A., Coe, R. S., et al. (2008). Constraints on the early uplift history of the Tibetan Plateau. Proceedings of the National Academy of Sciences of the United States of America, 105(13), 4987–4992. https://doi.org/10.1073/pnas.0703595105
- Wang, C. Y., Flesch, L. M., Silver, P. G., Chang, L. J., & Chan, W. W. (2008). Evidence for mechanically coupled lithosphere in central Asia and resulting implications. *Geology*, 36(5), 363–366. https://doi.org/10.1130/G24450A.1
- Xia, L., Li, X., Ma, Z., Xu, X., & Xia, Z. (2011). Cenozoic volcanism and tectonic evolution of the Tibetan Plateau. *Gondwana Research*, 19(4), 850–866. https://doi.org/10.1016/j.gr.2010.09.005
- Xu, T., Wu, Z., Zhang, Z., Tian, X., Deng, Y., Wu, C., & Teng, J. (2014). Crustal structure across the Kunlun fault from passive source seismic profiling in East Tibet. *Tectonophysics*, 627, 98–107. https://doi.org/10.1016/j.tecto.2013.11.010



- Ye, Z., Gao, R., Li, Q., Zhang, H., Shen, X., Liu, X., & Gong, C. (2015). Seismic evidence for the North China plate underthrusting beneath northeastern Tibet and its implications for plateau growth. *Earth and Planetary Science Letters*, 426, 109–117. https://doi.org/10.1016/j.epsl.2015.06.024
- Ye, Z., Li, J., Gao, R., Song, X., Li, Q., Li, Y., et al. (2017). Crustal and uppermost mantle structure across the Tibet-Qinling transition zone in NE Tibet: Implications for material extrusion beneath the Tibetan Plateau. *Geophysical Research Letters*, 44(20), 10,316–10,323. https://doi.org/10.1002/2017GL075141
- Yin, A., Dang, Y.-Q., Zhang, M., Chen, X.-H., & McRivette, M. W. (2008). Cenozoic tectonic evolution of the Qaidam basin and its surrounding regions (part 3): Structural geology, sedimentation, and regional tectonic reconstruction. *Geological Society of America Bulletin*, 120(7–8), 847–876. https://doi.org/10.1130/B26232.1
- Zhang, P., Shen, Z., Wang, M., Gan, W., Burgmann, R., Molnar, P., et al. (2004). Continuous deformation of the Tibetan Plateau from global positioning system data. *Geology*, 32(9), 809–812. https://doi.org/10.1130/G20554.1
- Zhang, Z., Bai, Z., Klemperer, S., Tian, X., Xu, T., Chen, Y., & Teng, J. (2013). Crustal structure across northeastern Tibet from wide-angle seismic profiling: Constraints on the Caledonian Qilian orogeny and its reactivation. *Tectonophysics*, 606, 140–159. https://doi.org/10.1016/j. tecto.2013.02.040
- Zhang, Z., Klemperer, S., Bai, Z., Chen, Y., & Teng, J. (2011). Crustal structure of the Paleozoic Kunlun orogeny from an active-source seismic profile between Moba and guide in East Tibet, China. *Gondwana Research*, 19(4), 994–1007. https://doi.org/10.1016/j.gr.2010.09.008
- Zhang, Z., Wang, Y., Houseman, G. A., Xu, T., Wu, Z., Yuan, X., et al. (2014). The Moho beneath western Tibet: Shear zones and eclogitization in the lower crust. *Earth and Planetary Science Letters*, 408, 370–377. https://doi.org/10.1016/j.epsl.2014.10.022
- Zheng, D., Li, H., Shen, Y., Tan, J., Ouyang, L., & Li, X. (2016). Crustal and upper mantle structure beneath the northeastern Tibetan Plateau from joint analysis of receiver functions and Rayleigh wave dispersions. *Geophysical Journal International*, 204(1), 583–590. https://doi.org/10.1093/qji/qqv469
- Zheng, X.-F., Yao, Z.-X., Liang, J.-H., & Zheng, J. (2010). The role played and opportunities provided by IGP DMC of China National Seismic Network in Wenchuan earthquake disaster relief and researches. *Bulletin of the Seismological Society of America*, 100(5B), 2866–2872. https://doi.org/10.1785/0120090257
- Zhu, L., & Helmberger, D. V. (1998). Moho offset across the northern margin of the Tibetan Plateau. Science, 281(5380), 1170–1172. https://doi.org/10.1126/science.281.5380.1170
- Zhu, L., & Kanamori, H. (2000). Moho depth variation in southern California from teleseismic receiver functions. *Journal of Geophysical Research*, 105(B2), 2969–2980. https://doi.org/10.1029/1999JB900322